

# Combined Circuit/Device Modeling and Simulation of Integrated Microfluidic Systems

Aveek N. Chatterjee and N. R. Aluru, *Member, IEEE*

**Abstract**—A combined circuit/device model for the analysis of integrated microfluidic systems is presented. The complete model of an integrated microfluidic device incorporates modeling of fluidic transport, chemical reaction, reagent mixing, and separation. The fluidic flow is generated by an applied electrical field or by a combined electrical field and pressure gradient. In the proposed circuit/device model, the fluidic network has been represented by a circuit model and the functional units of the  $\mu$ -TAS (micro Total Analysis System) have been represented by appropriate device models. We demonstrate the integration of the circuit and the device models by using an example, where the output from the fluidic transport module serves as the input for the other modules such as mixing, chemical reaction and separation. The combined circuit/device model can be used for analysis and design of entire microfluidic systems with very little computational expense, while maintaining the desired level of accuracy. [1237]

**Index Terms**—Circuit-modeling, lab-on-a-chip, microfluidics, simulation.

## I. INTRODUCTION

INTEGRATED microfluidic systems with a complex network of fluidic channels are often used for chemical and biochemical analysis [1], [2] as microfluidic devices offer unique advantages in sample handling, reagent mixing, chemical reaction, separation and detection. Computer-aided design (CAD) tools, when sufficiently fast, robust and accurate, can accelerate the design and development of integrated microfluidic systems. For example, using the CAD tools, microfluidic system designers will be able to quickly explore the design space and arrive at an optimal design before the system is fabricated.

Even though there are exceptions, an accurate description of the physical phenomenon in microfluidic devices is provided by the concepts of continuum theory, which couples the relevant mechanical and electro-dynamical quantities in terms of a (usually quite complex) system of partial differential equations. The solution of the partial differential equations (referred to as device modeling) can provide a detailed and accurate understanding of the device behavior, but device modeling is typically very expensive and tedious for microfluidic systems comprising hundreds of thousands of fluidic channels. Circuit or compact

modeling approaches are typically employed for integrated microfluidic system analysis and design, as these approaches are much faster compared to the device modeling techniques and are accurate enough to capture the fundamental physical characteristics and system behavior [3]–[6]. However, a compact or a circuit model may not be easily available for certain physical phenomena, in which case the use of device modeling becomes essential. In this paper, we report on appropriately combining circuit and device models for quick and accurate analysis of integrated microfluidic systems.

In an earlier paper [7], we reported on the development of a compact model for microfluidic transport due to a combined electric field and pressure gradient. The earlier model, however, did not account for a number of physical phenomena that are important within the electrical double layer for electrically-mediated fluid transport. In this paper, we first extend the earlier compact model for micro/nanofluidic transport due to a combined electric field and pressure gradient. Specifically, we have included capacitive elements to account for the electrical double layer, developed a complete circuit representation of the fluidic transport and developed models for no-slip flow, which can become important for fluid flow in nanometer scale channels, where the Debye length can be significant compared to the channel width. Second, we have combined the compact/circuit models for fluidic transport with device models for mixing, chemical reactions and separation to investigate analysis and design of micro total analysis systems ( $\mu$ -TAS). Finally, we apply the combined circuit/device modeling approach for analysis of large arrays of microfluidic channels to store fluids in an arbitrary pattern and for analysis of integrated microfluidic systems containing transport, mixing, reaction, detection and separation. The rest of the paper is organized as follows: Section II introduces a prototype integrated microfluidic system, which is used to explain the development of various compact/device models, Section III describes the development and integration of the circuit and device models for the various modules encountered in microfluidic systems, Section IV presents several examples of integrated microfluidic systems and their analysis by the combined circuit/device modeling approach and Section V presents conclusions.

## II. INTEGRATED MICROFLUIDIC SYSTEMS

The concept of a micro-Total Analysis System ( $\mu$ -TAS) or a lab-on-a-chip for integrated chemical and bio-chemical analysis has grown considerably in scope since its introduction [8], [9].  $\mu$ -TAS involves the miniaturization of all the functions found in chemical analysis, including fluidic transport, mixing, reaction and separation [10], so that the entire chemical measurement

Manuscript received December 31, 2003; revised July 23, 2004. This work was supported in part by the National Science Foundation under Grant ECS-0140496 and Grant CCR-0325344, and by the nano-CEMMS center at UIUC. Subject Editor R. R. A. Syms.

The authors are with the Department of Mechanical and Industrial Engineering, Beckman Institute for Advanced Science and Technology, University of Illinois at Urbana-Champaign, Urbana, IL 61801 USA (e-mail: aluru@uiuc.edu; Web: <http://www.uiuc.edu/~aluru>).

Digital Object Identifier 10.1109/JMEMS.2004.839025

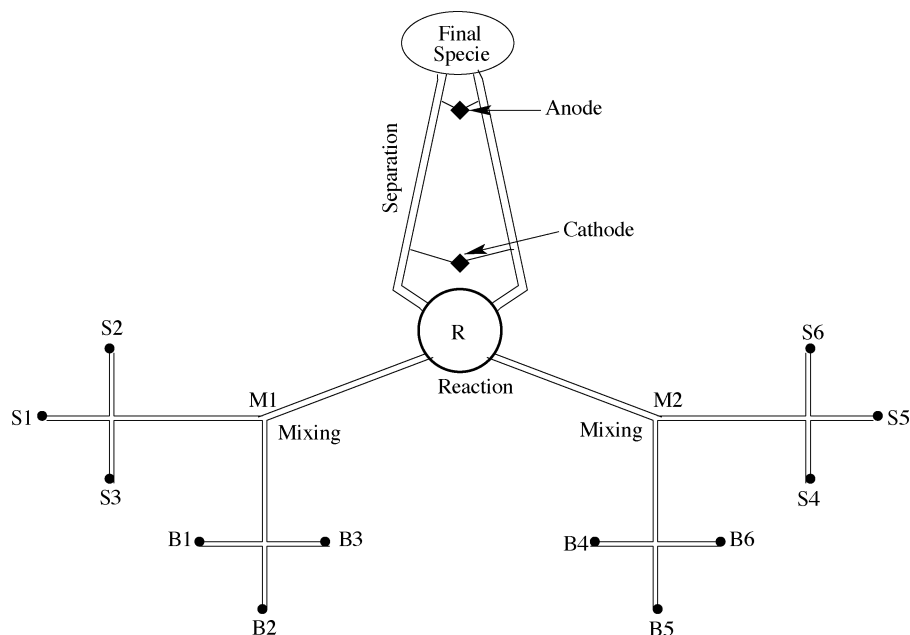


Fig. 1. Prototype chemical analysis system. The system incorporates fluidic transport, mixing, reaction and separation.

laboratory could be miniaturized onto a device of a few square centimeters. For example, the system shown in Fig. 1 incorporates the essential processes (fluidic transport, mixing, reaction and separation) involved in a  $\mu$ -TAS.

One of the critical elements of any microfluidic system or  $\mu$ -TAS is its fluidic transport system. For example, in Fig. 1, the fluid is transported from the ends of the cross-shaped segments to the reservoir marked as the “Final Specie”. Most microfluidic chips transport the fluid electrokinetically and/or by hydraulic pressure. Electrokinetic transport and control of fluids has the advantage that it eliminates the need for mechanically moving parts, such as valves and pumps, which have thus far been difficult to construct and interface to microchip systems [11].

An important element of the  $\mu$ -TAS is the reaction chamber. As shown in Fig. 1, chemical/biological species are transported to the reaction chambers, where chemical reactions take place leading to the formation of a product. The rate of formation of the product is dependent on the flux of the reactant, the proportion of the various reactants in the solution, the order of the reaction and the reaction kinetics. In those cases where online detection is not suitable, the solution from the reaction chamber may be transported to the detector for the purpose of off-chip detection [12]–[14]. If the detection of the product is easier or suitable than that of the reactant then the product is used for detection purpose as the concentration of the product can give quantitative information about the reacting species [15], [16]. Thus, often reaction and detection schemes are intrinsically linked together and both of these form an integral part of the  $\mu$ -TAS.

Another important functionality in  $\mu$ -TAS is the separation of bio-molecules and bio-chemical species. Electrophoresis [11] and isoelectric focusing [11] are the most commonly employed methods of separation. In Fig. 1, for example, the separation is based on electrophoresis. There are two separation channels carrying the same chemical species to the reservoir marked as the “Final Specie” from the micro-reactor (marked as “R”). In

both the separation channels, the flow is driven by electric field, which is created between the electrodes marked as the anode and the cathode in Fig. 1. One may obtain a greater flow rate by simultaneously transporting the required chemical species through two separation channels instead of one. The schematic proposed in Fig. 1 was inspired by an example of a device designed to perform 96 parallel electrophoretic separations reported by Shi *et al.* [17]. However, in the prototype a single set of electrophoretic separation system has been employed. Higher field intensity is generally tolerable for electrophoretic separation in a micro-channel because of the reduced influence of Joule heating (which reduces band broadening) in the micro-fabricated devices [18], [19]. Therefore, it is possible to obtain higher separation efficiency in a microdevice compared to a conventional capillary electrophoresis system [20]. Smaller characteristic dimensions in combination with higher field intensities lead to a shorter time scale of separation, which is a fundamental advantage in  $\mu$ -TAS compared with macroscopic devices.

When designing integrated microfluidic systems of the type shown in Fig. 1, some important objectives are to increase the throughput, improve the molecular homogeneity of the mixture [21], [22] and obtain higher separation efficiency and faster detection. However, it may not be possible to attain all these objectives and there can be a trade off leading to an optimized design. In the following sections, we develop and demonstrate an “easy-to-use” compact model, which can be used to explore the design space and select an optimal design for integrated microfluidic systems to perform various functions.

### III. MODEL DEVELOPMENT

The development of circuit and device models is illustrated using the example shown in Fig. 1. The models are, however, general enough that they can be applied/extended to other microfluidic systems. We first describe the development of compact/circuit model for fluid flow due to a combined pressure and

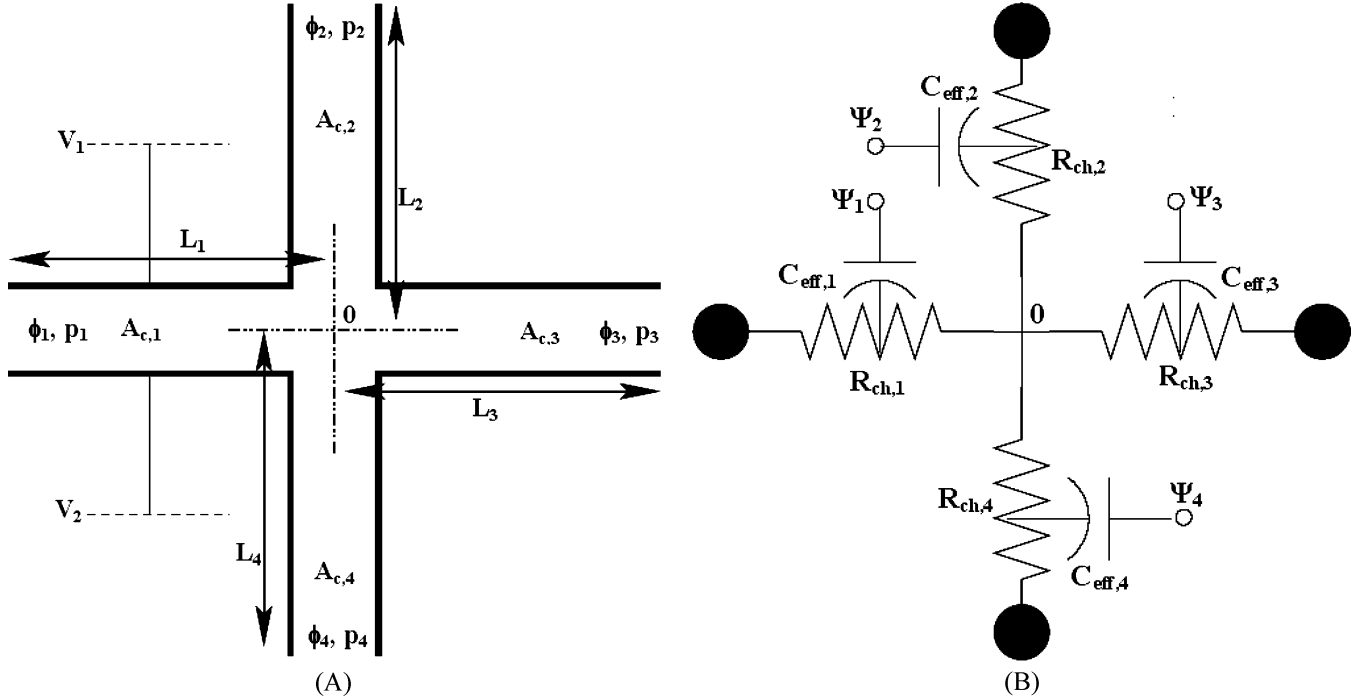


Fig. 2. (a) Typical cross-shaped channel segment of a microfluidic system. The electrical potentials  $\phi_{1-4}$ , and fluidic pressures,  $p_{1-4}$ , are given.  $V_1$  and  $V_2$  are the transverse applied potentials. (b) The electrical network representation for the cross-shaped channel.  $R_{ch,1-4}$  are the electrical resistances,  $\psi_{1-4}$  are the surface potentials of the channel walls and  $C_{eff,1-4}$  are the capacitances of the EDLs.

electrical potential gradient. The compact model is described in two parts—namely, the electrical model and the fluidic model.

#### A. Electrical Model

For microfluidic devices that rely on the electrokinetic force as the driving force, the electric field must be computed first. In the case of electroosmotic flow, the potential field due to an applied potential can be computed by solving the Laplace equation [23]

$$\nabla^2 \phi = 0 \quad (1)$$

where  $\phi$  is the electrical potential. Since (1) predicts a linear potential drop for simple straight channels, the potential variation can be represented by linear electrical resistances. In order to develop a complete circuit that takes into account the charge stored in the electrical double layer (EDL), capacitive elements also need to be included while modeling the electrical domain. The EDL can be decomposed into the Stern layer and the diffuse layer [24]. As the Stern layer and the diffuse layer store charge, the capacitance associated with these layers is important. In addition, the capacitance of the channel wall, which arises due to a potential difference across the channel wall, needs to be taken into account. The electrical resistance of the EDL can be safely neglected as the effective resistance of the EDL is much higher than the resistance of the channel filled with buffer [25]. Fig. 2(a) and Fig. 2(b) illustrate a typical cross-shaped channel segment (this is similar, for example, to the cross-shape formed by S1, S2, M1, S3 in Fig. 1) in a microfluidic system and its circuit representation in the electrical domain, respectively.

The electrical resistance of a solution filled simple straight channel is given by the following expression:

$$R_{ch,i} = \frac{\rho_{sol,i} L_i}{A_{c,i}} \quad (2)$$

where  $\rho_{sol,i}$  is the electrical resistivity of the solution in the  $i$ th channel,  $i = 1, 2, \dots, 4$  [see Fig. 2(b)],  $L_i$  is the length of the  $i$ th channel,  $A_{c,i}$  is the cross-sectional area of the  $i$ th channel and  $R_{ch,i}$  is the electrical resistance of the  $i$ th channel.

The expression for the effective capacitance, shown in Fig. 2(b), is given by

$$(C_{eff,i})^{-1} = (C_{st,i})^{-1} + (C_{dl,i})^{-1} + (C_{wall,i})^{-1} \quad (3)$$

where  $C_{st,i}$  is the capacitance of the Stern layer of the  $i$ th channel,  $C_{dl,i}$  is the capacitance of the diffuse layer of the  $i$ th channel and  $C_{wall,i}$  is the capacitance of the  $i$ th channel wall.  $C_{st,i}$  is given by the following expression [24]:

$$C_{st,i} = \frac{\varepsilon A_{s,i}}{x_{H,i}} \quad (4)$$

where  $\varepsilon$  is the permittivity of the fluid in the channel,  $A_{s,i}$  is the inner surface area of the  $i$ th channel and  $x_{H,i}$  is the thickness of the Stern layer. The capacitance of the diffuse layer,  $C_{dl,i}$ , is given by the following expression [26]:

$$C_{dl,i} = \frac{\sigma_{T,i} A_{s,i}}{\left[ \left( \frac{2k_b T}{ze} \right) \sinh^{-1} \left( \sigma_{T,i} \sqrt{\left[ \frac{500\pi}{\varepsilon R T c} \right]} \right) \right]} \quad (5)$$

where  $\sigma_{T,i}$  is the intrinsic surface charge density on the channel wall,  $k_b$  is the Boltzmann's constant,  $T$  is the temperature,  $z$  is the valence of the counter-ion,  $e$  is the charge of an electron,  $c$

is the concentration of the counter ion in the bulk solution and  $R$  is the universal gas constant.

The capacitance of the wall for a cylindrical channel,  $C_{wall,i}$ , is given by the following expression [27]:

$$C_{wall,i} = \frac{\varepsilon A_{s,i}}{r_i \log\left(\frac{r_o}{r_i}\right)} \quad (6)$$

where  $r_i$  is the inner radius of the channel and  $r_o$  is the outer radius of the channel.

When no potential difference is applied across the channel wall, no charge is induced on the channel wall. As a result the capacitance of the channel wall can be neglected in the computation of the effective capacitance. For example, there is no wall capacitance for  $i = 2, 3, 4$  as there is no applied voltage across the channel as shown in Fig. 2(a). Typically, the capacitance of the Stern layer is much higher compared to the capacitance of the diffuse layer [24]. Also, when capacitances are connected in series (as in this case) the capacitance with the smaller value dominates. Therefore, in most cases the effective capacitance,  $C_{eff}$ , can be approximated by the diffuse layer capacitance,  $C_{dl}$ . The effective capacitance can be related to the surface potential by the expression:

$$C_{eff,i} \psi_{0,i} = q_{st,i} = \sigma_{T,i} A_{s,i} \quad (7)$$

or

$$\psi_{0,i} = \frac{\sigma_{T,i} A_{s,i}}{C_{eff,i}} \quad (8)$$

where  $\psi_{0,i}$  is the surface potential on the  $i$ th channel and  $q_{st,i}$  is the total charge stored in the EDL of the  $i$ th channel.

### B. Fluidic Model

For the fluidic transport driven by an electrical field and/or a pressure gradient, the “through quantities” are the flow rates through the channels and the “across quantities” are the electrical potential differences and the pressure differences imposed on the fluidic channels. In this section we present a derivation of the constitutive equation relating the “through quantities” to the “across quantities”. The flow field of a fully developed incompressible flow in a microfluidic device is governed by the continuity equation (9) and the steady-state momentum equation (10) [28], i.e.

$$\nabla \cdot \mathbf{u} = 0 \quad (9)$$

$$(\mathbf{u} \cdot \nabla) \mathbf{u} = \frac{\mu}{\rho} \nabla^2 \mathbf{u} - \frac{\nabla p}{\rho} + \frac{\mathbf{F}}{\rho} \quad (10)$$

where  $\mathbf{u}$  is the velocity vector,  $\mathbf{F}$  is the body force vector,  $p$  is the pressure,  $\rho$  is the density of the fluid, and  $\mu$  is the dynamic viscosity. For electroosmotic flow, the body force term,  $\mathbf{F}$  in (10), is obtained by solving the Poisson–Boltzmann equation [23].

1) *Slip Case*: The slip case model can be used when the thickness of the EDL is insignificant compared to the depth or diameter of the channel. The body force,  $\mathbf{F}$ , is nonzero only within a few Debye lengths from the channel wall as the potential induced by the zeta potential drops to zero very quickly near

the channel wall [23]. In the development of the compact model for the slip flow case, we will assume that the flow is fully developed and the thickness of the EDL is insignificant compared to the thickness or diameter of the channel (this assumption usually holds good for channels larger than 200 nm). As a result, the effect of the electrokinetic force can be represented by a slip velocity at the wall given by the Helmholtz–Smoluchowski equation [2]:

$$u_{slip} = -\frac{\varepsilon \zeta}{\mu} \nabla \phi \quad (11)$$

where  $\mu$  is the dynamic viscosity of the fluid,  $\nabla \phi$  is the potential gradient across the fluidic channel, and  $\zeta$  is the zeta potential on the surface of the fluidic channel. The Poisson–Boltzmann equation, which is used for the full-scale simulation of electroosmotic flow, can be linearized for low values of surface charge density. Then, the Debye–Huckel theory [2] predicts the following relationship between the zeta potential,  $\zeta$ , and the surface potential,  $\psi_0$

$$\zeta = \psi_0 \exp(-\kappa \chi) \quad (12)$$

where  $\kappa$  is the inverse of the Debye length and  $\chi$  is the radius of the counter ion. The surface potential can be computed from (8) by using the capacitance model. Thus, from knowing the surface potential, the zeta potential of the channel wall can be computed. The velocity profile across a capillary slit is a function of only the slip velocity and the pressure gradient, i.e.

$$u = -\frac{1}{2\mu} \frac{dp}{dx} \left( y^2 - \frac{h^2}{4} \right) + u_{slip} \quad (13)$$

where  $x$  denotes the stream direction of the channel,  $y$  denotes the transverse direction of the channel, and  $h$  is the channel depth. Since  $u_{slip}$  is given by (11), solving for the velocity in (13) is reduced to computing the pressure distribution in the fluidic network. By taking the divergence of the momentum equation [(10)] and applying the continuity condition, we get the following expression:

$$\nabla^2 p = \nabla \cdot \mathbf{F} - \nabla \cdot (\rho (\mathbf{u} \cdot \nabla) \mathbf{u}). \quad (14)$$

In the regions where the flow is fully developed, the convection term  $(\mathbf{u} \cdot \nabla) \mathbf{u}$  is zero. Thus,  $\nabla \cdot (\rho (\mathbf{u} \cdot \nabla) \mathbf{u})$  vanishes. The term corresponding to the divergence of the force must be zero in the fully developed flow regions. Otherwise, the flow would not be fully developed due to the nonuniform body force. Hence, for the region where the flow is fully developed, the pressure calculation is reduced to a Laplace equation

$$\nabla^2 p = 0. \quad (15)$$

Thus, (15) decouples the solution of pressure from the solution of velocity.

Integrating the velocity profile given in (13) across the cross-section of the capillary slit and using (1), (11) and (15), we get the following expression for the flow rate per unit width:

$$Q = \left( \frac{h^3}{12\mu L} \right) \Delta p + \left( \frac{\varepsilon \zeta h}{\mu L} \right) \Delta \phi. \quad (16)$$

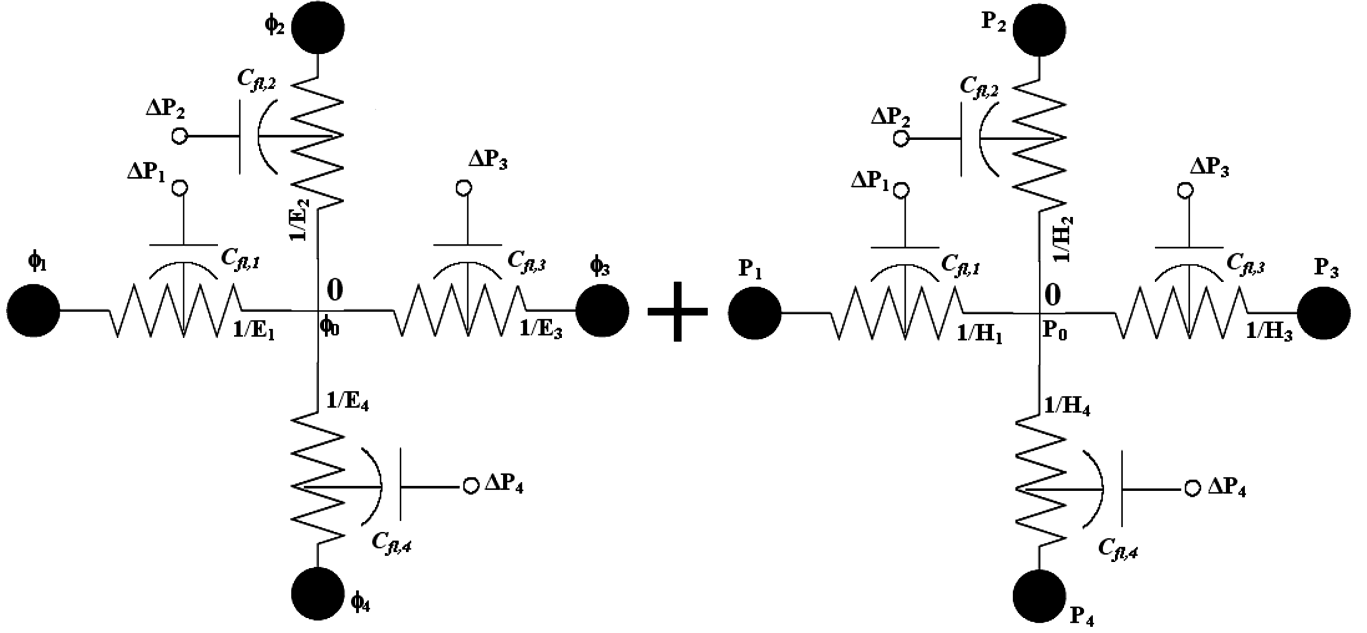


Fig. 3. Circuit representation for the electrokinetically driven flow is on the left.  $E_{1-4}$  are the electrohydraulic conductances of the channels and ( $C_{fl,1-4}$ ) are the fluidic capacitances.  $\Delta P_{1-4}$  are the pressure differences (which are the across quantities in the fluidic domain) across the fluidic capacitances. Circuit representation for the pressure driven flow is given on the right.  $H_{1-4}$  are the hydraulic conductances of the channels. The “plus” sign between the two figures indicates that the total flow is the sum of the electrokinetically driven flow and the pressure driven flow.

For the  $i$ th channel in an array of channels, (16) can be rewritten as

$$Q_i = H_i \Delta p_i + E_i \Delta \phi_i \quad (17)$$

where  $H_i$  is the hydraulic conductance of the  $i$ th channel,  $E_i$  is the electrohydraulic conductance of the  $i$ th channel,  $\Delta p_i$  is the pressure drop in the  $i$ th channel and  $\Delta \phi_i$  is the electrical potential drop in the  $i$ th channel. The expressions for  $H_i$  and  $E_i$  for the capillary slit are given in (16). For a cylindrical channel, the hydraulic conductance and the electrohydraulic conductance (corresponding to the flow rate) are given by

$$H_i = \frac{\pi r_i^4}{8\mu_i L_i} \quad (18)$$

$$E_i = \frac{\varepsilon \zeta_i \pi r_i^4}{\mu_i L_i} \quad (19)$$

where  $r_i$  is the inner radius of the  $i$ th cylindrical channel. Equation (17) is the constitutive relationship, which relates the “through quantity” to the “across quantities” (a combined pressure and electrical potential drop). If the flow is driven by only a pressure gradient, then the second term in (16) can be neglected. Similarly, if the flow is driven by only an electric field, then the first term on the right-hand side of (16) can be neglected. Fig. 3 shows the circuit representations of the fluidic domain for the cross-shaped channel segment shown in Fig. 2(a). Note that the total flow is the sum of the electrokinetically driven flow and the pressure driven flow.

2) *No-Slip Case*: The slip velocity model discussed above can be employed when the Debye length is thin compared to the channel width. However, when the Debye length is comparable to the channel width, the slip velocity model may not be

accurate. For a capillary slit, the velocity profile is given by the following expression [29]:

$$u = -\frac{1}{2\mu} \frac{dp}{dx} \left( y^2 - \frac{h^2}{4} \right) - \frac{\varepsilon}{\mu} \nabla \phi (\psi_0 - \psi) \quad (20)$$

where

$$\psi = \frac{\psi_0 \cosh\left(\frac{y}{\lambda_D}\right)}{\cosh\left(\frac{h}{\lambda_D}\right)} \quad (21)$$

$\lambda_D$  is the Debye length and is given by the following expression [7]:

$$\lambda_D = \sqrt{\frac{\varepsilon RT}{2Fc^2c}} \quad (22)$$

where  $c$  is the intrinsic ionic concentration of the fluid in the absence of an electrical potential and  $F_c$  is the Faraday’s constant. Integrating the velocity profile [given in (20)] across the cross section and using (21), we get the following expressions for the hydraulic conductance and the electrohydraulic conductance of the  $i$ th channel

$$H_i = \frac{h_i^3}{12\mu_i L_i} \quad (23)$$

$$E_i = \frac{\varepsilon}{\mu_i L_i} \psi_0 \left[ 2h_i - 2\lambda_D \frac{\sinh\left(\frac{h_i}{\lambda_D}\right)}{\cosh\left(\frac{h_i}{\lambda_D}\right)} \right]. \quad (24)$$

Similarly, expressions for the hydraulic conductance and the electrohydraulic conductance of a cylindrical channel can also be derived [29].

3) *Fluidic Channels With Elastic Membranes*: In case of channels with integrated elastic parts in them (e.g., a flexible membrane) a capacitive element needs to be included in the circuit model of the fluidic domain as shown in Fig. 3. The fluidic capacitor can be modeled as

$$C_{fl} = \frac{\int_{\Gamma} w(x, y) d\Gamma}{p} \quad (25)$$

where  $C_{fl}$  is the fluidic capacitance,  $w$  is the deflection,  $\Gamma$  is the total surface area of the flexible membrane and  $p$  is the pressure difference across the channel wall. For a rectangular membrane of dimension  $a \times b$ , the fluidic capacitance from (25) is given by

$$C_{fl} = \frac{4a}{\pi^5 D_{\text{rigidity}}} \sum_{m=1,3,5,\dots}^{\infty} \frac{(-1)^{\frac{m-1}{2}} \sin\left(\frac{m\pi}{2}\right)}{m^5 \frac{m\pi}{a}} \times \left[ \frac{b}{2} + \frac{a}{2m\pi} \{ \alpha_m - \tanh(\alpha_m) (3 + \alpha_m \tanh(\alpha_m)) \} \right] \quad (26)$$

where

$$\alpha_m = \frac{m\pi b}{2a} \quad (27)$$

$D_{\text{rigidity}}$  is the rigidity of the membrane and is given by

$$D_{\text{rigidity}} = \frac{E_{\text{mod}} \delta_{th}^3}{12(1-\nu^2)} \quad (28)$$

$\delta_{th}$  is the thickness of the membrane,  $E_{\text{mod}}$  is the elastic modulus of the membrane, and  $\nu$  is the Poisson's ratio of the membrane.

The implementation of the electrical model and the fluidic model is carried out using the modified nodal analysis technique [30]. Once the variation of  $\phi$  and  $p$  is known the flow rate in each channel can be computed using the constitutive relationship given in (17).

### C. Chemical Reactions: Device Models

Consider a scheme in which the chemical species  $A$  and  $B$  are transported to the reaction chamber, where they undergo a second-order reversible reaction process to produce species  $C$ . The governing equations for this reaction process are given by



$$\frac{\partial m_A}{\partial t} = Q_A C_A - k_1(m_A)(m_B) + k_2(m_C) \quad (30)$$

$$\frac{\partial m_B}{\partial t} = Q_B C_B - k_1(m_A)(m_B) + k_2(m_C) \quad (31)$$

$$\frac{\partial m_C}{\partial t} = k_1(m_A)(m_B) - k_2(m_C) \quad (32)$$

where  $Q_i$  is the flow rate of the  $i$ th specie, which is computed from the fluidic transport model (or known from the design specifications),  $C_i$  is the concentration of the  $i$ th specie,  $m_i$  is the number of moles of the  $i$ th species present in the reaction chamber,  $k_1$  is the forward reaction rate and  $k_2$  is the backward reaction rate.

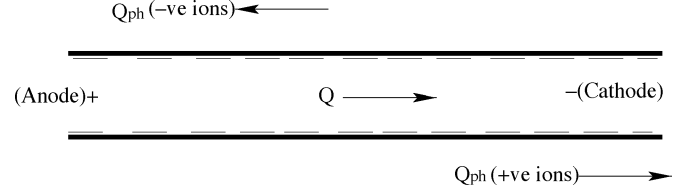


Fig. 4. Basic separation unit, which can separate species that are oppositely charged, have different valence or different electrophoretic mobility.

A trapezoidal scheme is used to discretize the ODE's given in (30) to (32). The discretized equations are given by

$$\frac{(m_A^{n+1} - m_A^n)}{\Delta t} = Q_A C_A - \frac{k_1}{4} (m_A^{n+1} + m_A^n) (m_B^{n+1} + m_B^n) + \frac{k_2}{2} (m_C^{n+1} + m_C^n) \quad (33)$$

$$\frac{(m_B^{n+1} - m_B^n)}{\Delta t} = Q_B C_B - \frac{k_1}{4} (m_A^{n+1} + m_A^n) (m_B^{n+1} + m_B^n) + \frac{k_2}{2} (m_C^{n+1} + m_C^n) \quad (34)$$

$$\frac{(m_C^{n+1} - m_C^n)}{\Delta t} = \frac{k_1}{4} (m_A^{n+1} + m_A^n) (m_B^{n+1} + m_B^n) - \frac{k_2}{2} (m_C^{n+1} + m_C^n). \quad (35)$$

The nonlinear equations (33)–(35) are solved by employing a Newton–Raphson scheme to compute  $m_A^{n+1}$ ,  $m_B^{n+1}$ , and  $m_C^{n+1}$  at the  $(n+1)$ th time step given  $m_A^n$ ,  $m_B^n$ , and  $m_C^n$  at the  $n$ th time step. Equations (33)–(35) comprise the device model for the reaction module.

### D. Separation: Device Model

Fig. 4 shows a simple separation mechanism, which is repeated as the basic unit in the circular separation device reported by Kutter [31]. The separation unit can separate species that are either oppositely charged, have different valence or different electrophoretic mobility.

The total flux of a given species through a channel is given by the following expression:

$$J_t = \left[ D_{\text{diff}} \frac{\partial c}{\partial x} + \frac{z F_c D_{\text{diff}}}{RT} (\nabla \phi) c + v_{\text{conv}} c \right] A_c \quad (36)$$

where  $J_t$  is the total flux,  $D_{\text{diff}}$  is the diffusion coefficient of the specie,  $c$  is the concentration of the specie,  $F_c$  is the Faraday's constant,  $z$  is the valence of the ion,  $R$  is the universal gas constant,  $T$  is the temperature,  $A_c$  is the cross-sectional area of the fluidic channel and  $v_{\text{conv}}$  is the convective velocity of the flow that arises due to the bulk flow rate,  $Q$ , given in (16)

$$v_{\text{conv}} = \frac{Q}{A_c}. \quad (37)$$

From (36), the total flux is the sum of the diffusive flux (given by the first term), the electrophoretic flux (given by the second term and it is zero for uncharged species) and the convective flux (given by the last term), which arises due to the bulk flow in the channel. Typically, the separation unit is designed in such a way that the convective flux and the electrophoretic flux (for charged species) dominate over the diffusive flux [32]. Thus, assuming

that the diffusive flux is negligible, the expression for the total flux is given by

$$J_t = \left[ \frac{zF_c D_{\text{diff}}}{RT} (\nabla \phi) c + v_{\text{conv}} c \right] A_c \quad (38)$$

or

$$J_t = (Q_{ph} + Q) c \quad (39)$$

where  $Q$  is the convective flow rate, which is computed using (16) and  $Q_{ph}$  is the electrophoretic flow rate, which is given by the following expression [32]:

$$Q_{ph} = \left[ \frac{zF_c D_{\text{diff}}}{RT} \right] A_c \nabla \phi. \quad (40)$$

Thus, the constitutive equation, which relates the ‘‘through quantity’’ (electrophoretic flow rate) to the ‘‘across quantity’’ (electrical potential difference), in the case of electrophoretic flow, is given by

$$Q_{ph} = \left[ \frac{zF_c D_{\text{diff}}}{RT} \frac{A_c}{L} \right] \Delta \phi = \mathcal{F} \Delta \phi \quad (41)$$

where  $\mathcal{F}$  is the electrophoretic conductance of the fluidic channel.

Consider an example, where two species  $A$  and  $B$  are present in the separation channel shown in Fig. 4. Assume that species  $A$  is unit-positively charged and species  $B$  is unit-negatively charged, while the surface of the channel has a negative fixed charge. Therefore, the electroosmotic flow through the channel would be from left to right (i.e., from the anode side to the cathode side) as shown in the Fig. 4. The electrophoretic flow for  $A$  would be from left to right but that for  $B$  would be in the opposite direction. This is due to the difference in the electrophoretic velocity of these two species. Thus, the ratio of the rate of molar increment at the outlet of the separation channel for the two species is given by the following expression:

$$\begin{aligned} \text{Separation Ratio} &= \frac{(Q + \text{sign}(z_A) \times |Q_{ph}|_A) c_A^{\text{in}}}{(Q + \text{sign}(z_B) \times |Q_{ph}|_B) c_B^{\text{in}}} \\ &= \frac{(Q + |Q_{ph}|_A) c_A^{\text{in}}}{(Q - |Q_{ph}|_B) c_B^{\text{in}}} \end{aligned} \quad (42)$$

where  $c_A^{\text{in}}$  is the concentration of species  $A$  at the inlet and  $c_B^{\text{in}}$  is the concentration of species  $B$  at the inlet. Considering that the bulk flow is due to electrical potential gradient only (i.e., pressure driven flow is absent), the separation ratio of the species can be expressed in terms of the electrophoretic conductance, electro-hydraulic conductance and the inlet concentration of the species, i.e.

$$\text{Separation Ratio} = \frac{(E + \mathcal{F}_A) c_A^{\text{in}}}{(E + \mathcal{F}_B) c_B^{\text{in}}}. \quad (43)$$

Thus, the knowledge of the electrophoretic conductance and the electrohydraulic conductance can be used to compute the separation ratio using (43), which can be considered as the device model for the separation module.

### E. Integration of the Models

Algorithm 1 summarizes the integration of the circuit and device models for the prototype integrated microfluidic system shown in Fig. 1. The circuit based electrical model is first employed to compute the electrical potential distribution in the entire microfluidic system. Using the electrical potential distribution as an input, the fluidic circuit model is used to compute the fluidic variables (e.g., the pressure distribution, flow rate, etc.) in the entire system. The flow rates through various channels are then used to compute the mixing ratio/efficiency, reactions and the separation ratio. Even though Algorithm 1 is specific to the microfluidic system shown in Fig. 1, it can be generalized to various other microfluidic systems by appropriately combining the electrical, fluidic, mixing, reaction/detection and separation modules.

**Algorithm 1** A Procedure for computing the variables of a micro/nanofluidic chip

1. Define the electrical circuit and the fluidic circuit using the principles described in Sections III-A and -B.
2. Compute the electrical potential distribution ( $\{\phi\}$ ) and the fluidic pressure distribution ( $\{p\}$ ).
- for** each channel  $i = 1, 2, \dots, N$ : where,  $N$  is the number of fluidic channels. **do**  
 Compute  $R_{ch,i}$  (equation (2)),  $C_{\text{eff},i}$  (equation (3)),  $H_i$  [see (18)] and  $E_i$  [see (19)].  
**end for**
- Solve for the nodal electrical potential and the nodal fluidic pressure using the modified nodal analysis technique.
3. Compute the flow rate.
- for**  $i = 1, 2, \dots, N$ : where,  $N$  is the number of fluidic channels. **do**  
 Compute  $Q_i$  (the flow rate in the  $i$ th channel) using (17)  
**end for**
4. Compute the effectiveness of mixing.
- for**  $i = 1, 2, \dots, M$ : where,  $M$  is the number of fluidic channels where mixing is taking place. **do**  
 Compute the effectiveness of mixing,  $e_{\text{mix}}$  using the model given by (45).  
**end for**
5. Compute the molar concentration in the reaction chamber.
- for**  $j = 1, 2, \dots, R$ : where,  $R$  is the number of reaction chambers. **do**  
 Initialize the number of moles of the various species in every reaction chamber.  
**for**  $n = 0, 1, \dots, T_f$ : where,  $T_f$  is the final time. **do**  
**repeat**  
 Guess,  $\mathbf{m}^i$ , compute  $\mathbf{f}_{\text{res}}^i$ , and the Jacobian,  $\mathbf{J}^i$ .

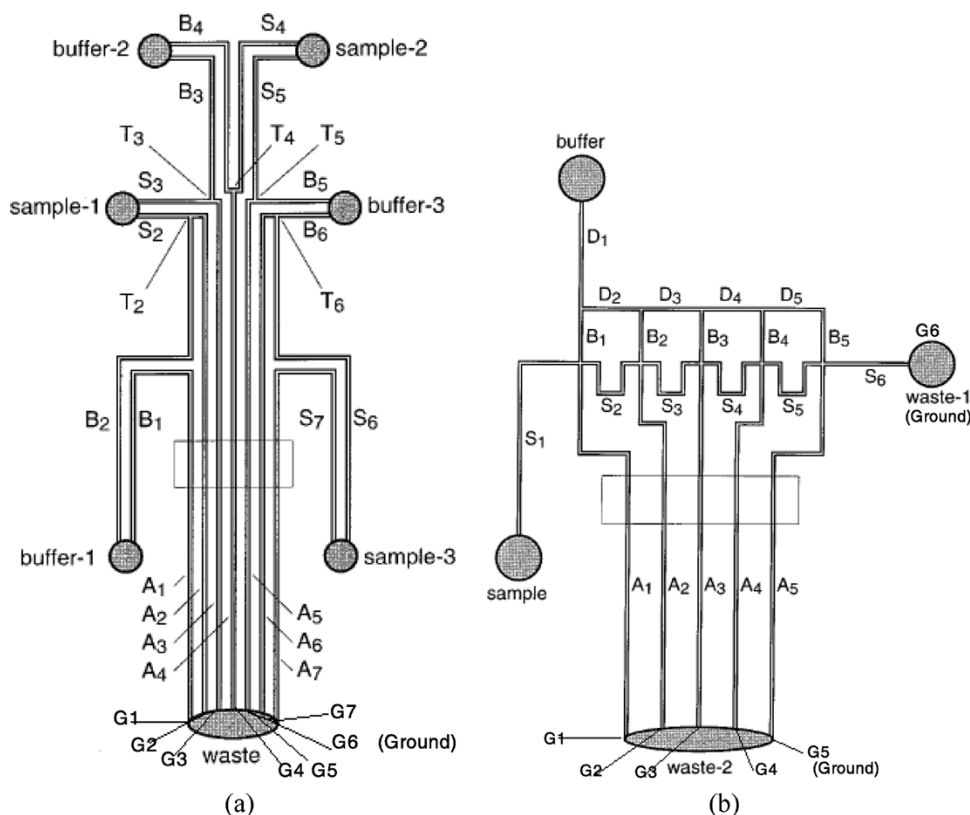


Fig. 5. Schematics of the microchips for parallel (a) and serial (b) electrokinetic mixing. The circles depict sample, buffer and waste reservoirs. The sample, buffer and analysis channels are labeled “S,” “B,” and “A,” respectively. The T intersections are the basic units for the parallel mixing device, while the cross intersections are the basic units for the serial mixing device [33].

```

Solve for  $\Delta m^i$ ; compute  $m^{i+1} = m^i + \Delta m^i$ .
until convergence. (Convergence check
is  $|\Delta m^i| \leq \text{TOLERANCE}$ )
end for
end for
6. Compute the separation ratio.
for  $i = 1, 2, \dots, S$ : where,  $S$  is the number of
separation channels. do
Compute the electrophoretic conductance
of the relevant species using (41) and
retrieve the inlet
concentration of the relevant species.
Compute the separation ratio at the
outlet of the channel using (43).
end for

```

#### IV. RESULTS

We have considered several examples from the literature [7], [33]–[35] to verify and analyze the combined circuit/device model. In this section, we demonstrate the application of the models and the implementation using some key examples. In the first example (Fig. 5, [33]), we consider microfluidic devices, which can be used for electrokinetically driven parallel and serial mixing. In the second example, we demonstrate a circuit model based analysis of a pneumatically controlled fluidic transport system, which has been used in a high density

microfluidic chip by Quake *et al.* [36]. In the final example, we consider an integrated system, and a complete simulation based analysis of the lab-on-a-chip has been demonstrated.

##### A. Example 1: Electrokinetically Driven Mixing

Microfluidic devices for parallel and serial mixing have been experimentally demonstrated by Jacobson *et al.* [33]. The parallel mixing device [see Fig. 5(a)] is designed with a series of independent T-intersections, and the serial mixing device [see Fig. 5(b)] is based on an array of cross-intersections. Figs. 6 and 7 show the circuit representation of the mixing devices. As the channels do not contain any flexible walls, the fluidic capacitances are neglected. The parameters (e.g., channel dimensions and applied potential) used in the simulation are the same as those used in the experiments reported in [33]. The zeta potential of the channel walls for this example is computed from the capacitor model and has been verified with the experimental results given in [33]. Thus, the inclusion of the capacitance in the new circuit model proposed in this paper can provide the zeta potential and the surface potential required for computing the slip flow or the no-slip flow. The expressions that have been used to compute the sample fraction are the same as those given in [33].

Table I gives a comparison of the simulated and experimental results for the parallel mixing device and Table II gives a comparison of the simulated and experimental results for the serial mixing device. The simulation results show very good agreement with the experimental results. The CPU times to compute

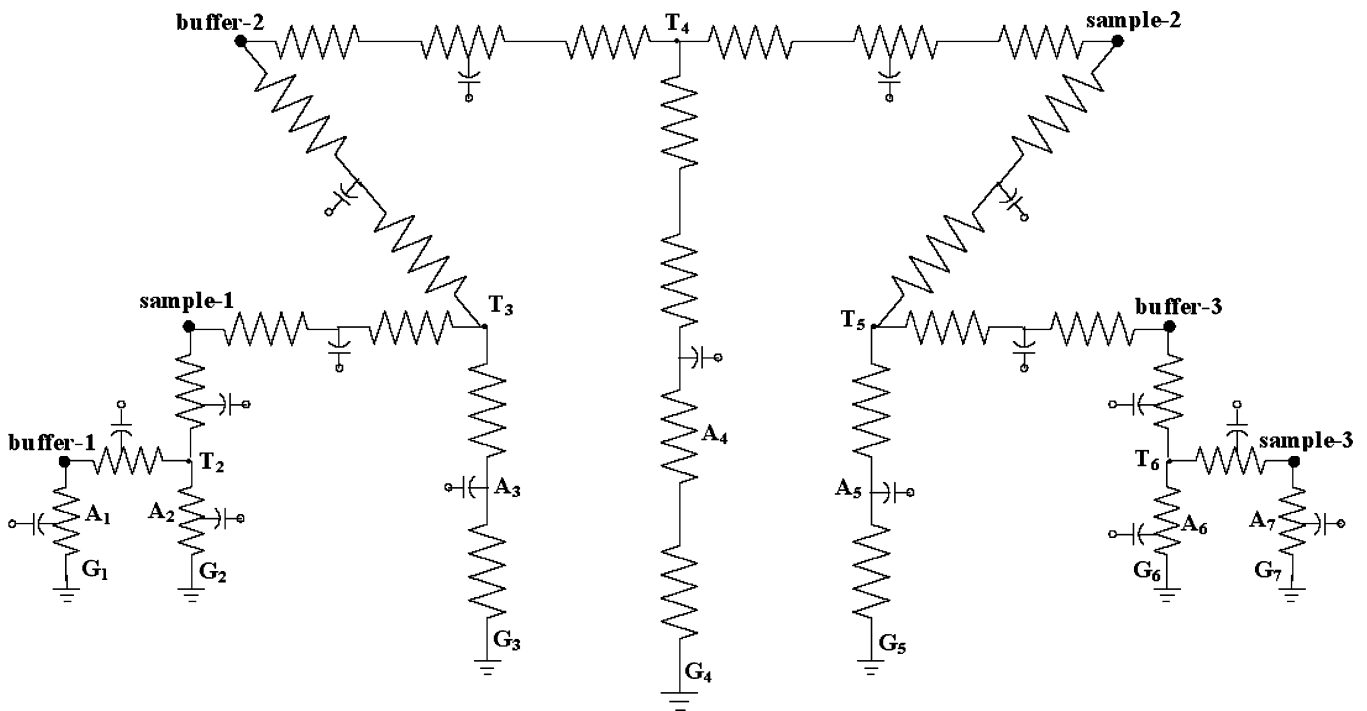


Fig. 6. The circuit (both fluidic and electrical) representation of the parallel mixing device. Since the flow is electrokinetic driven, the fluidic resistance of the channel is the inverse of the electrohydraulic conductance.

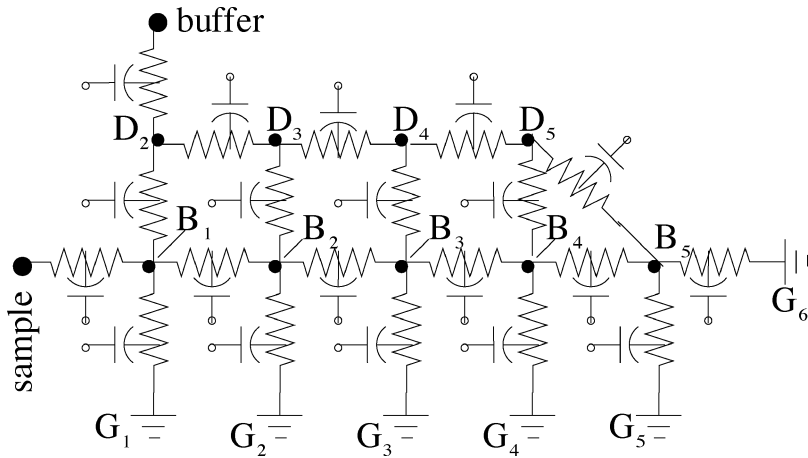


Fig. 7. The circuit representation of the serial mixing device.

TABLE I  
A COMPARISON OF THE SIMULATED AND EXPERIMENTAL RESULTS FOR PARALLEL MIXING

CHANNEL	SAMPLE FRACTION (EXPERIMENTAL)	SAMPLE FRACTION (SIMULATION)
A <sub>1</sub>	0	0
A <sub>2</sub>	0.84	0.833
A <sub>3</sub>	0.67	0.675
A <sub>4</sub>	0.51	0.522
A <sub>5</sub>	0.36	0.340
A <sub>6</sub>	0.19	0.165
A <sub>7</sub>	1.0	1.0

the electrical variables and the fluidic variables for the systems shown in Fig. 5 (i.e., the mixing devices) were of the order of 1 second. Fig. 8(a) and (b) show the variation in the sample frac-

tion that can be obtained by controlling the electrical potential at the buffer and the sample reservoirs. These results demonstrate the advantage of the circuit model for designing microfluidic

TABLE II  
A COMPARISON OF THE SIMULATED AND EXPERIMENTAL RESULTS FOR SERIAL MIXING

CHANNEL	SAMPLE FRACTION (EXPERIMENTAL)	SAMPLE FRACTION (SIMULATION)
$A_1$	1.0	1.0
$A_2$	0.36	0.37
$A_3$	0.21	0.22
$A_4$	0.12	0.12
$A_5$	0.059	0.053

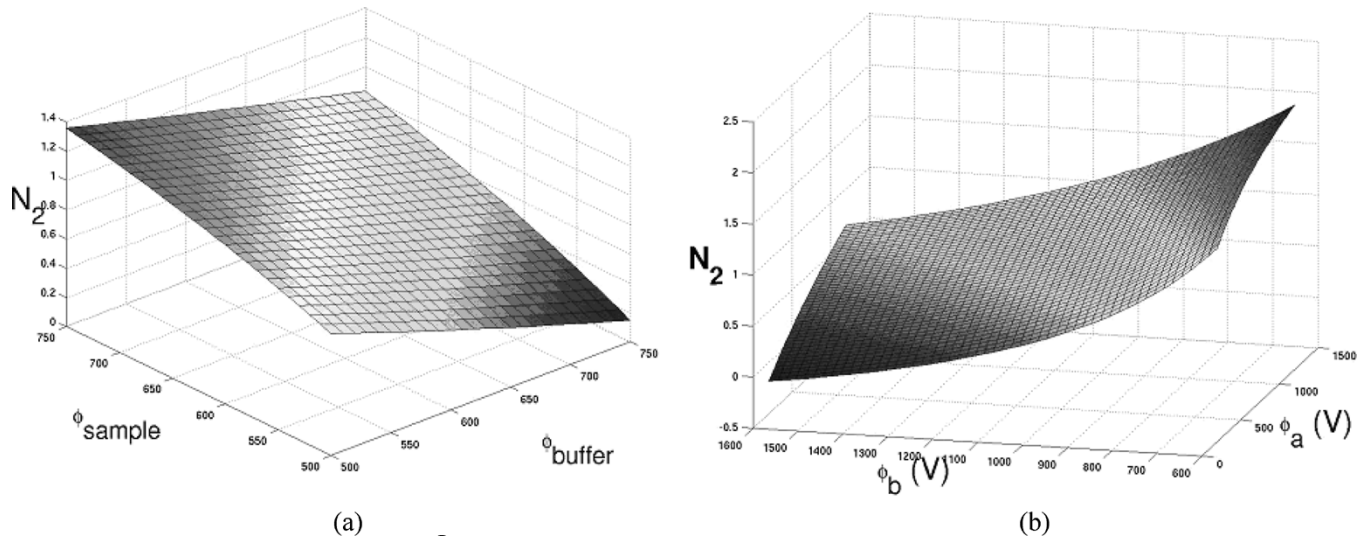


Fig. 8. Variation in the sample fraction of the 2nd analysis channel when the applied potential (in “Volts”) in the sample reservoir and the buffer reservoir is changed. The plots for the other analysis channels (in both cases) have the same pattern. (a) Parallel mixing and (b) serial mixing.

systems. It is practically impossible to get the variation of the output parameter with the input parameter varying over such a large range, by using experimental techniques or full-scale simulation methods.

The depth of the channels considered for parallel and serial mixing are  $10\ \mu\text{m}$  and  $5.5\ \mu\text{m}$ , respectively. For such large depths, the slip flow circuit model presented in Section III-B1 gives accurate results. Even if a no-slip flow circuit model is employed, the results would match exactly with the slip flow circuit model. However, as the depth of the channel gets smaller, the no-slip model can produce more accurate results compared to the slip-flow model. Shown in Fig. 9 is a comparison of the relative error between the full simulation results and the slip and no-slip models for channel depths of 50, 100, and 200 nm. The Debye length is 10 nm in all the cases. For both the models, the error grows as the depth of the channel decreases. However, the error is much smaller with the no-slip model compared to the slip model. Also, the rate of growth of the error is smaller with the no-slip model compared to the slip model.

### B. Example 2: Large Scale Integration

In the large scale integration based microfluidic chip designed by Quake *et al.* [36], the fluidic transport system consists of two layers (Fig. 1 in [37])—the “control” layer, which contains all channels required to actuate the valves, is situated on top of the “flow” layer and the “flow” layer contains the network of the channels being controlled [37]. A valve is created whenever a

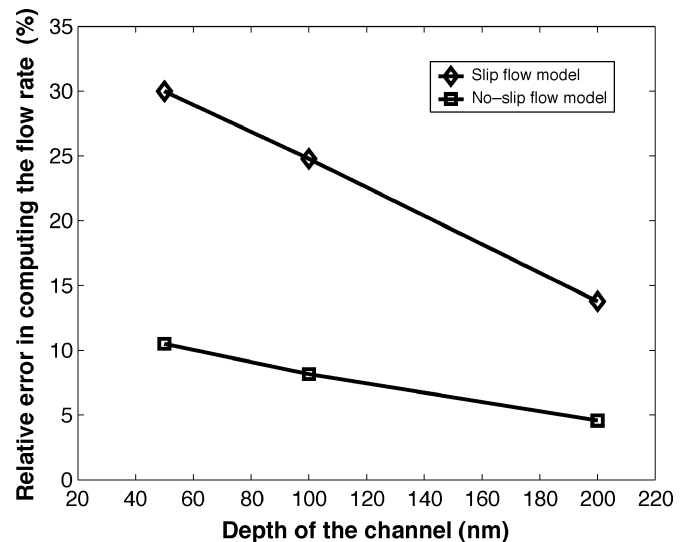


Fig. 9. Comparison of the percentage relative error in the bulk flow rate  $Q$  between the slip flow model and the no-slip flow model when compared with full-scale simulation.

control channel crosses a flow channel. The resulting thin membrane at the junction between the two channels can be deflected by fluidic actuation [36], [37]. The schematic *A* of Fig. 1 in [37] shows the orientation of the control layer and the flow layer. The schematic *B* of Fig. 1 in [37] shows the valve closing for rectangular and rounded channels. In Fig. 10(a) the “top-view” of

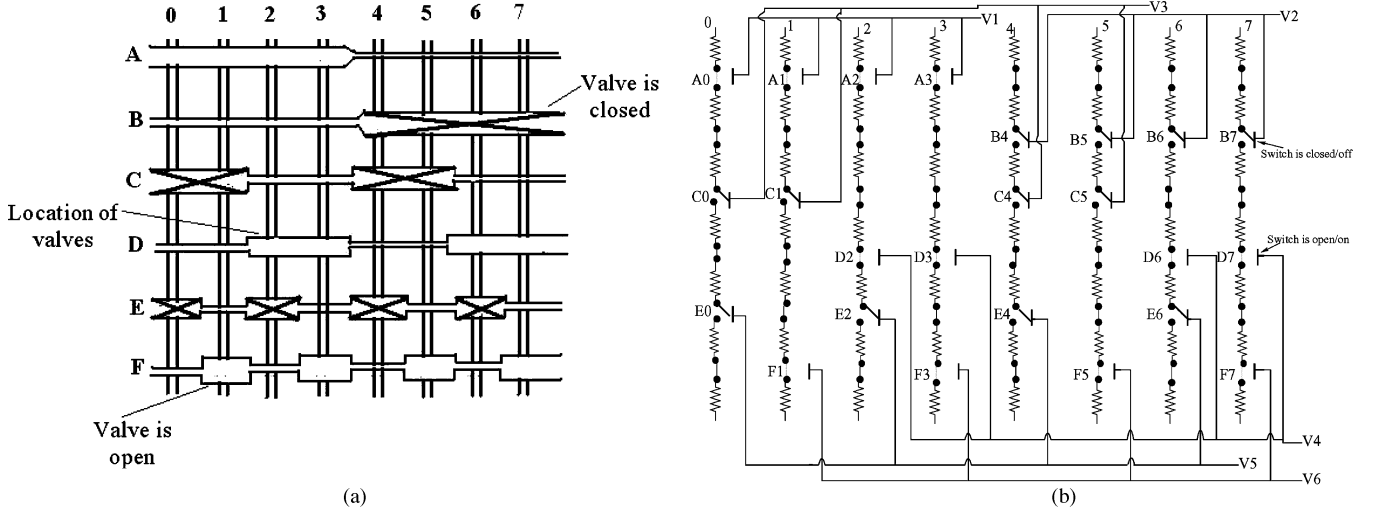


Fig. 10. (a) Microfluidic system consisting of “control channels” (left to right) and “flow channels” (top to bottom). Intersections with wider control channels denote valves or switches. A cross indicates a closed valve. For further details refer to [36]. (b) The fluidic circuit representation of the system shown in (a). The valves are modeled as electrical switches.

the device is given, where the black channels oriented from west to east are the control channels and the gray channels oriented from north to south are flow channels. The control layer is on top of the flow layer. The flow channels are numbered from 0 to 7 and the control channels are named in the alphabetic order from *A* to *F*. A valve at the intersection of flow channel 0 and control channel *A* is designated as “A0.” Such a designation is later used to explain the circuit representation of the system. The configuration shown in Fig. 10(a) consists of simple on-off valves, which can be considered as fluidic switches to control the flow in the “flow” channels. Each control line can actuate multiple valves simultaneously. As the dimension of the control line can be varied, it is possible to have a control line pass over multiple flow channels to actuate multiple valves. The active element is the roof of the flow channel and the intersections, which act as valves or fluidic switches are denoted by a wider width of the control channel. The intersections, which are marked by a cross [see Fig. 10(a)], indicate a closed (or off) position and the intersections, which are not marked by any cross, indicate an open (or on) position. The circuit representation for the microfluidic system shown in Fig. 10(a) [36] is depicted in Fig. 10(b). Since the flow is pressure driven, only the fluidic circuit needs to be considered. The fluidic circuit represents the flow layer and the intersections with valves are shown as electrical switches. The resistances (or conductances) in the fluidic circuit of Fig. 10(b) are the fluidic resistances of the channels in the flow layer. The on-off position of the valves depends on the gauge pressure in the control channel compared to the pressure in the flow channel. Thus, the control layer is represented in the fluidic circuit through its gauge pressure. In Fig. 10(b) the

pressure difference of the  $i$ th control channel is represented by “ $V_i$ ”. The notation “ $V$ ” is used because of the analogy between electrical voltage and pressure. The on position of a switch [in Fig. 10(b)] is represented by a vertical dash connecting two consecutive resistances (e.g., “A0”) and the off position of a switch is represented by a slanted dash causing a break between two consecutive resistances (e.g., “B4”). The hydraulic conductances (or hydraulic resistances) can be modeled using the approach explained in Section III. The pressure actuated control valves can be modeled as switches, which are considered “off” if the pressure in the control channel is above the “threshold pressure” and are considered “on” if the pressure in the control channel is below the threshold pressure. The threshold pressure can be computed from (44) shown at the bottom of the page [38] where  $h$  is the height of the flow channel,  $a$  and  $b$  are the dimensions of the rectangular membrane acting as the valve,  $D_{\text{rigidity}}$  is the rigidity of the membrane [given by (28)] and  $\alpha_m$  is given by (27). Fig. 11(a) shows the simulated flow distribution in the flow layer of the microfluidic circuit shown in Fig. 10(b). A “plus” sign corresponding to a given flow channel indicates that the flow is “on”; otherwise the flow is “off”. A cell associated with a given flow channel will receive fluid only if the flow is on. The nonlinear variation of the threshold pressure with the thickness of the membrane and with the dimension of the square membrane can be utilized for optimizing the design of the fluidic switch. The CPU time to simulate the flow distribution for the system shown in Fig. 10 was 16 s.

Fig. 11(b) shows the simulation result for an array of  $60 \times 126$  chambers. Fluid is stored in the chambers based on the filling mechanism described in Fig. 10 [36]. This result demonstrates

$$P_{\text{threshold}} = \frac{\left(\frac{ha}{2}\right)}{\left[\frac{4a^4}{\pi^5 D_{\text{rigidity}}} \sum_{m=1,3,5,\dots}^{\infty} \frac{(-1)^{\frac{m-1}{2}} \sin\left(\frac{m\pi}{2}\right)}{m^5 \frac{m\pi}{a}} \left(1 - \frac{\alpha_m \tanh(\alpha_m) + 2}{2 \cosh(\alpha_m)}\right)\right]} \quad (44)$$

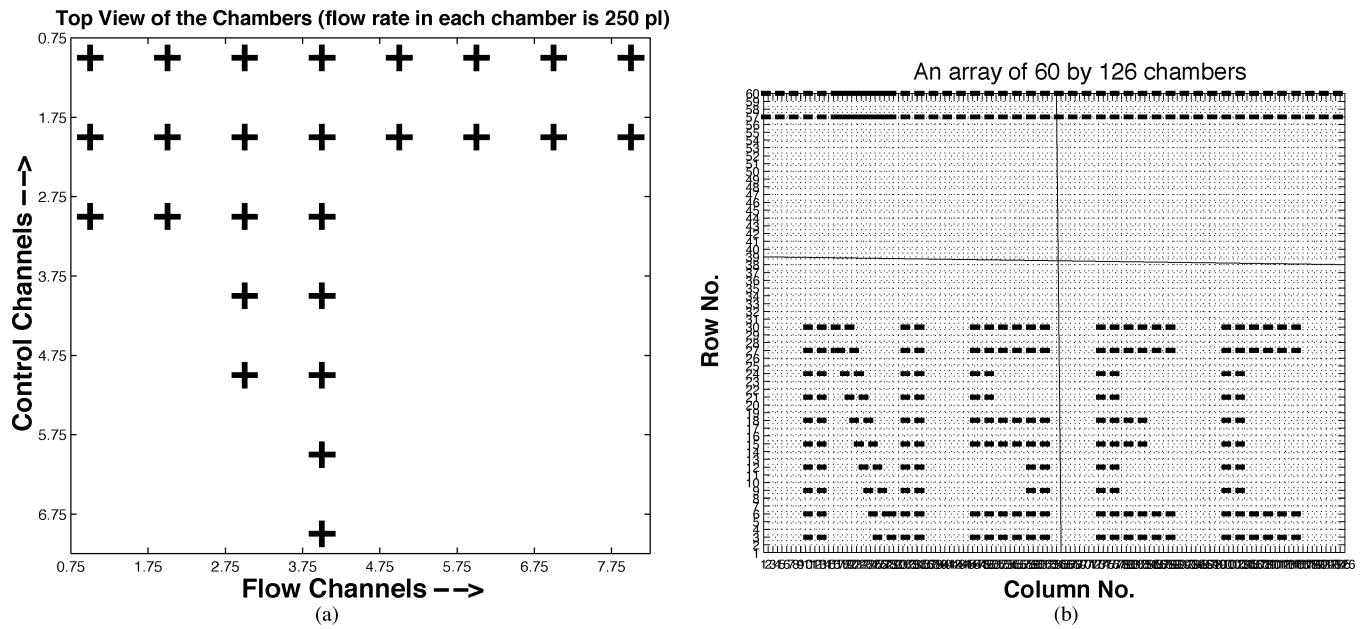


Fig. 11. (a) Simulation of fluid flow through the microfluidic system shown in Fig. 10. The plus signs indicate presence of flow. (b) An example of large scale integration, where the fluid is stored in a desired pattern in a microfluidic chip containing  $60 \times 126$  chambers.

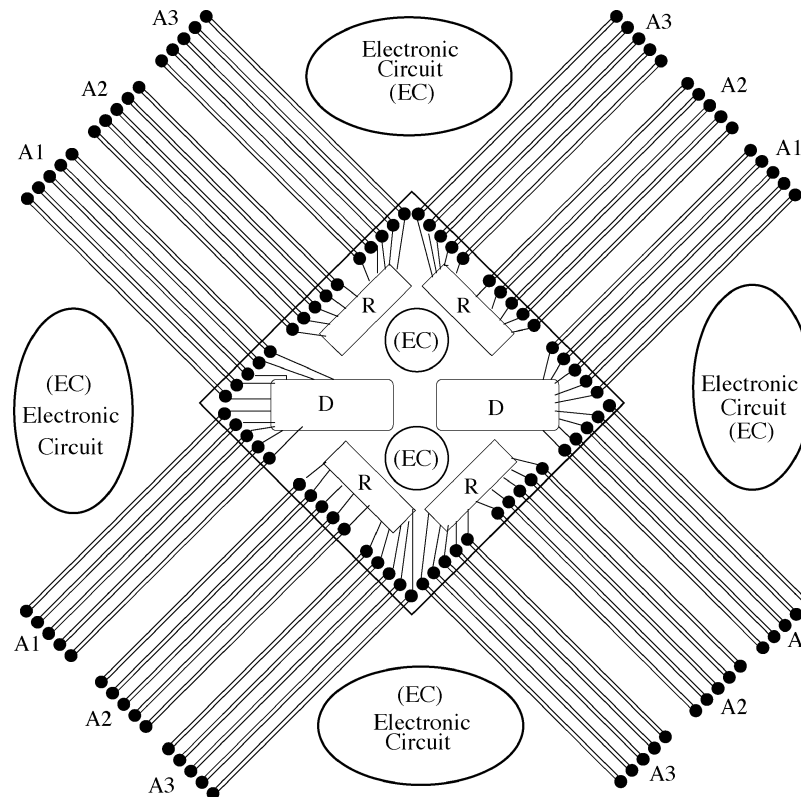


Fig. 12. The schematics of the microfluidic chip considered in the final example. The fluidic transport system represented on the south-west side of the chip is duplicated on all the other sides.

that the fluid can be stored in any arbitrary pattern using large scale integration of micro/nanochannels.

### C. Example 3: Lab-on-a-Chip

In the final example we consider a lab-on-a-chip system (see Fig. 12), which is designed based on the “Nanochip” reported

by Becker *et al.* [39]. The various chemical species are transported to the different modules on the chip from their sources by using electrokinetic transport. One third of the channels (marked as set A1 in Fig. 12) perform the dual role of fluid transport and passive mixing. Each channel in the set marked as A1 is designed as shown in Fig. 13 [31]. In this design,



Fig. 13. The split channel design used for fluid transport in set *A1* of the microfluidic chip. This type of channel serves a dual purpose of transporting and mixing. In this example, a split level of 3 has been used.

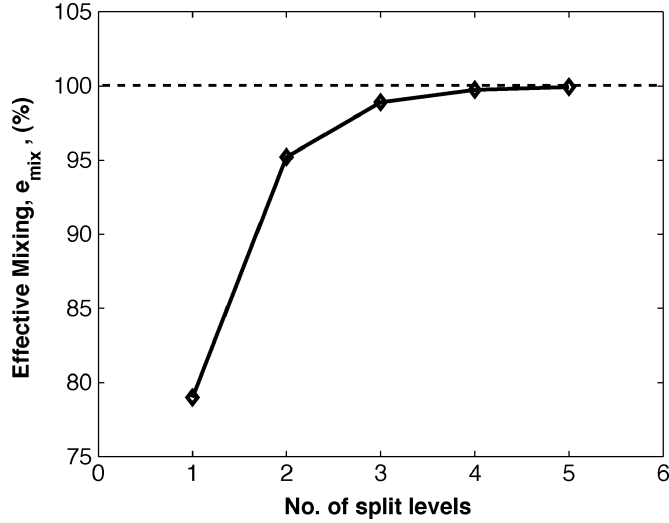


Fig. 14. The dependence of the effectiveness of the mixing (i.e., homogeneity of the mixture) on the number of split levels used.

the characteristic dimension at a given level is half of that at the previous level. As a result, in the case of diffusion dominated mixing [40], the equilibration time for mixing decreases at every level as the equilibration time for homogenous mixing is proportional to the square of the characteristic dimension. Thus, the molecular homogeneity of the sample being transported increases. In the simulations presented here, the number of splitting levels is considered as a design parameter. Fig. 14 shows the dependence of the molecular homogeneity of the mixture,  $e_{\text{mix}}$ , on the number of split levels. The mixing effectiveness is defined as [21]:

$$e_{\text{mix}} = 1 - \frac{\sqrt{\frac{1}{N} \sum_{i=1}^N (c_i - c_i^{PM})^2}}{\sqrt{\frac{1}{N} \sum_{i=1}^N (c_i^0 - c_i^{PM})^2}} \quad (45)$$

where  $c_i$  is the concentration at the  $i$ th node,  $c_i^{PM}$  is the concentration at the  $i$ th node if the two streams (i.e., the sample and the buffer streams) are perfectly mixed and  $c_i^0$  is the concentration at the  $i$ th node if the two streams do not mix at all. The analytical solution of the diffusion equation, obtained by the method of separation of variables, provides the concentration variation in the transverse direction. The mixing effectiveness,  $e_{\text{mix}}$ , ranges from 0 to 1, with 1 indicating complete mixing and 0 indicating no mixing.

The following parameters have been used for the results shown in Figs. 14 and 15(a):  $\Delta\phi = 100$  V (the potential

difference is applied between the start and the end of the channel, e.g., in Fig. 13 it is applied between 0 and 11); length of each level =  $200 \mu\text{m}$  (the length of each split level is kept constant ( $200 \mu\text{m}$ ) as the number of split levels are changed); height of the initial channel =  $16 \mu\text{m}$ ;  $\sigma_T = 6.2 \times 10^{-3} \text{ C/m}^2$ ;  $\mu = 10^{-3} \text{ kg/m.s}$ ;  $\varepsilon = 6.95 \times 10^{-10}$ . The concentration of species *A* at the inlet of the transport system is considered to be 0.1 mM.

Electrophoretic separation and electrokinetic transport is the governing mechanism through the set of channels marked as *A2* (in Fig. 12), while electrokinetic transport is the governing mechanism through the set of channels marked as *A3*. The species in set *A1* (say *A*) is transported to the detection module (*D*), where it reacts with species *B* (already present in the detection chamber) to produce species *C*, which can be used for off-chip detection. The reaction model given in (33) to (35) has been used to simulate the reaction between species *A* and *B* to produce species *C*. The initial condition corresponds to zero moles of *A* and *C* and one mole of species *B* in the reaction chamber (*D*). A second order forward reaction is considered for this reaction chamber (i.e., *D*). Therefore, the backward reaction rate is considered to be zero. A forward reaction rate of  $10^{-2} (\text{mM} \cdot \text{s})^{-1}$  has been considered. Fig. 15(a) shows the variation in the rate of formation of species *C* with time for different applied potentials. If the minimum concentration of species *C* required for detection is known (say 1 mM as considered in this case), then one can predict the detection time from the simulation results or one can design the chip to meet a specific detection time.

The chambers at the inlet of channels *A2* consists of two chemical species, *G* and *W*. The chemical species *G* is the useful reactant which reacts with the chemical species *H* (transported through the channels *A3*) in the reactor module (*R* in Fig. 12), where they undergo a second order reversible chemical reaction to produce another chemical specie, *F*. The reaction model given in (33) to (35) has been used for simulating the reaction between species *G* and *H* to produce species *F*. The initial condition corresponds to zero moles of *G*, *H* and *F* in the reaction chamber (*R*). The following parameters have been used for this phase: total length of a single channel = 2 mm; height of a single channel =  $1 \mu\text{m}$ ;  $\sigma_T = 2 \times 10^{-1} \text{ C/m}^2$ ; forward reaction rate =  $0.1 (\text{mM} \cdot \text{s})^{-1}$ ; backward reaction rate =  $0.01 \text{ s}^{-1}$ . At the inlet of the transport system, the concentration of species *G* is considered to be 20 mM, and the concentrations of species *W* and *H* are considered to be 50 mM. Fig. 15(b) shows the effect of different number of input ports on the variation of the concentration of *F* with time. In Fig. 12 the number of input ports per species is 5. Fig. 16 shows the dependence of the separation ratio (taking place in the set “A2”) on the ratio of the electrophoretic mobility of the species (in this case, the ratio of the electrophoretic mobility of species *W* to that of species *G*) being separated. The separation ratio is the ratio of the flux of species *G* to that of species *W*. The applied potential difference is 100 V for this case. A time step of 0.1 s has been used for this case. The CPU time to do a transient analysis of the complete system (shown in Fig. 12) for 500 s was of the order of 10 min.

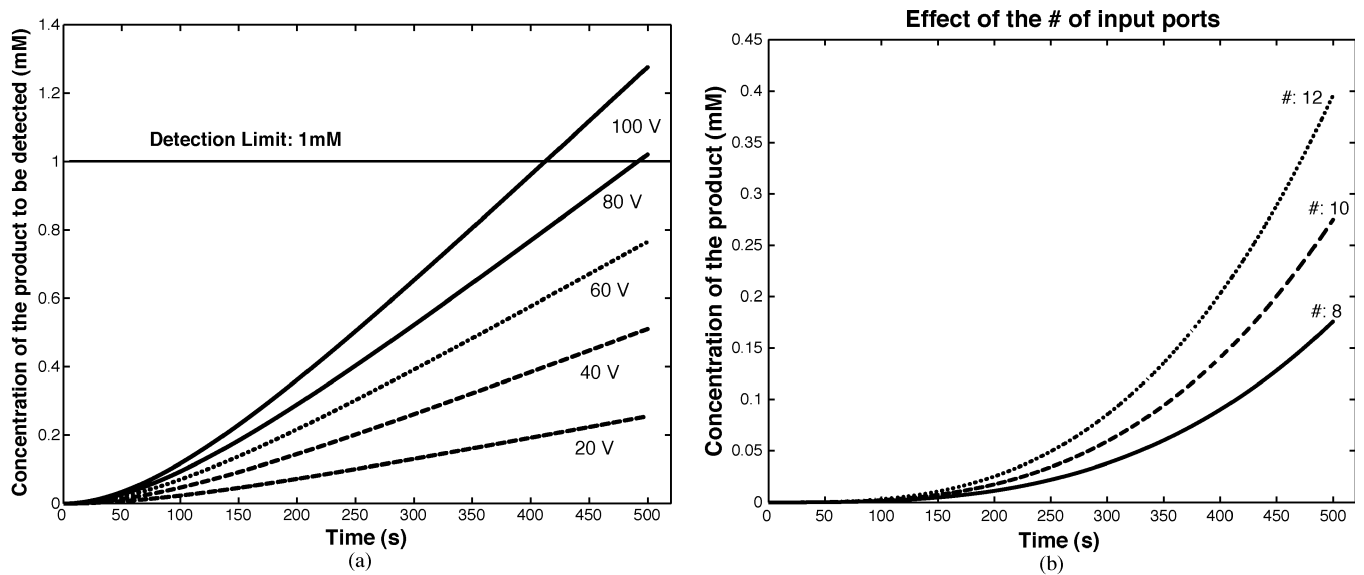


Fig. 15. (a) Concentration (of species  $C$ ) versus time for various applied potentials. (b) Concentration (of species  $F$ ) versus time for different numbers of input ports per side of the microfluidic chip.

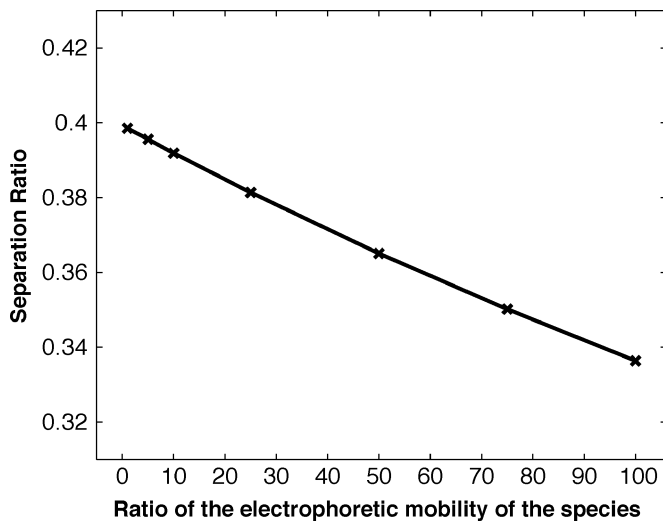


Fig. 16. The dependence of separation ratio (taking place on set "A2" in Fig. 12) on the ratio of the electrophoretic mobility of the species being separated.

## V. CONCLUSION

An advanced compact model for fluidic transport in microfluidic systems is presented. The new circuit/compact model for the fluidic transport accounts for a number of additional elements (such as capacitors to account for the electrical double layer and models for no-slip flow), that were neglected in the model presented earlier by Qiao *et al.* [7]. As a result, the circuit model presented in this paper can capture the physics of the fluidic transport process in much greater detail. In the results section, we have demonstrated the advantages of including the capacitance in the circuit model and the use of the no-slip flow fluidic circuit model for nanometer scale channels, where the Debye length is significant compared to the channel depth. We have also presented device models for other significant modules, such as chemical reaction chambers and separation channels, and discussed the integration of the device models with the

circuit models for analysis of micro-TAS. The results obtained from the circuit/device model show very good agreement with the experimental results and previously published simulation results [7], [33], [36]. The complete analysis of the lab-on-a-chip considered in the final example underscores the practical advantages of the combined circuit/device model, which can simulate the entire system much faster than a full scale model. The combined circuit/device model presented in this paper can be used to simulate and design future generation very large scale integrated (VLSI) micro/nano-fluidic chips.

## REFERENCES

- [1] R. Chien and J. W. Parce, "Multiport flow-control system for lab-on-a-chip microfluidic devices," *Fresenius' J. Anal. Chem.*, vol. 371, pp. 106–111, 2001.
- [2] R. F. Probstein, *Physicochemical Hydrodynamics*. New York: Wiley, 1994.
- [3] J. E. Vandermeer, M. S. Kanz, and G. K. Fedder, "Electroosmotic capillary flow with nonuniform zeta potential," *Anal. Chem.*, vol. 72, pp. 1053–1057, 1998.
- [4] J. Wu and L. R. Carley, "Table based numerical macromodeling for MEMS devices," in *Technical Proc. 2001 Int. Conf. on Modeling and Simulation of Microsystems (Hilton Head Island, SC, March 2001)*, 2001, pp. 68–71.
- [5] G. Casinovi, "Efficient simulation of MEMS using element stamps," in *Technical Proc. 2001 Int. Conf. on Modeling and Simulation of Microsystems (Hilton Head Island, SC, March 2001)*, 2001, pp. 112–115.
- [6] P. Voigt, G. Schrag, and G. Wachutka, "Microfluidic system modeling using VHDL-AMS and circuit simulation," *Microelectron. J.*, vol. 29, pp. 791–797, 1998.
- [7] R. Qiao and N. R. Aluru, "A compact model for electroosmotic flows in microfluidic devices," *J. Micromech. Microeng.*, vol. 12, pp. 625–635, 2002.
- [8] A. Manz, N. Graber, and H. M. Widmer, "Miniaturized total chemical analysis systems: a novel concept for chemical sensing," *Sens. Actuators B, Chem.*, vol. 1, pp. 244–248, 1990.
- [9] D. J. Harrison, K. Fluri, K. Seiler, Z. Fan, C. Effenhauser, and A. Manz, "Micromachining a miniaturized capillary electrophoresis-based chemical analysis system on a chip," *Science*, vol. 261, pp. 895–897, 1993.
- [10] P. A. Greenwood and G. M. Greenway, "Sample manipulation in micro total analytical systems," *Trends Anal. Chem.*, vol. 21, pp. 726–740, 2002.
- [11] B. H. Weigl, R. L. Bardell, and C. R. Cabrera, "Lab-on-a-chip for drug development," *Adv. Drug Del. Rev.*, vol. 55, pp. 349–377, 2003.

- [12] J. Ng, I. Gitlin, A. Strook, and G. Whitesides, "Components for integrated poly(dimethylsiloxane) microfluidic systems," *Electrophoresis*, vol. 23, pp. 3461–3473, 2002.
- [13] B. K. Gale, K. D. Caldwell, and A. B. Frazier, "Electrical conductivity particle detector for use in biological and chemical micro-analysis systems," in *Proc. SPIE Symposium on Micromachining and Microfabrication: Micro Fluidic Devices and Systems (Santa Clara, CA)*, vol. 3515, 1998, pp. 230–242.
- [14] A. J. Pfeiffer, T. Mukherjee, and S. Hauan, "Design and optimization of compact microscale electrophoretic separation system," *ACS Ind. Eng. Chem. Res.; ASAP Web Release Date: 03-Apr-2004*, vol. 47, pp. A–O, 2004.
- [15] P. D. Fletcher, S. Haswell, and X. Zhang, "Electrokinetic control of a chemical reaction in a lab-on-a-chip micro-reactor: measurement and quantitative modeling," *Lab on a Chip*, vol. 2, pp. 102–112, 2002.
- [16] T. Lee, M. Carles, and I. Hsing, "Microfabricated PCR-electrochemical device for simultaneous DNA amplification and detection," *Lab on a Chip*, vol. 3, pp. 100–105, 2003.
- [17] Y. Shi, P. C. Simpson, J. R. Scherer, D. Wexler, C. Skibola, M. T. Smith, and R. A. Mathies, "Radial capillary array electrophoresis microplate and scanner for high-performance nucleic acid analysis," *Anal. Chem.*, vol. 71, pp. 5354–5361, 1999.
- [18] N. Petersen, R. Nikolajsen, K. Mogensen, and J. Kutter, "Effect of joule heating on efficiency and performance for microchip-based and capillary based electrophoretic separation systems: a closer look," *Electrophoresis*, vol. 25, pp. 253–269, 2004.
- [19] N. Petersen, K. Mogensen, and J. Kutter, "Performance of an in-plane detection cell with integrated waveguides for UV/Vis absorbance measurements on microfluidic separation device," *Electrophoresis*, vol. 23, pp. 3528–3536, 2002.
- [20] W. Ehrfeld, "Electrochemistry and microsystems," *Electrochimica Acta*, vol. 48, pp. 2857–2868, 2003.
- [21] P. Huang and K. S. Breuer, "Performance and scaling of an electroosmotic mixer," in *The 12th International Conference on Solid-State Sensors, Actuators and Microsystems (Transducers 2003)*, Boston, MA, 2003, pp. 663–667.
- [22] P. Huang, "Electro-Osmotic Mixing in Microchannels," Sc. M. Thesis, Brown University, 2002.
- [23] M. Mitchell, R. Qiao, and N. R. Aluru, "Meshless analysis of steady state electroosmotic transport," *J. Microelectromech. Syst.*, vol. 9, pp. 435–449, 2000.
- [24] K. B. Oldham and J. C. Myland, *Fundamentals of Electrochemical Science*. San Diego, CA: Academic, 1994.
- [25] M. A. Hayes and A. J. Ewing, "Electroosmotic flow control and monitoring with an applied radial voltage for capillary zone electrophoresis," *Anal. Chem.*, vol. 64, pp. 56–62, 2000.
- [26] J. T. Davies and E. K. Rideal, *Interfacial Phenomena*. London, U.K.: Academic, 1966.
- [27] E. N. Lurch, *Fundamentals of Electronics*. New York: Wiley, 1971.
- [28] F. M. White, *Fluid Mechanics*: McGraw-Hill, 2002.
- [29] J. C. Colburn and P. D. Grossman, *Capillary Electrophoresis: Theory and Practice*. New York: Academic, 1992.
- [30] J. Ogrodzki, *Circuit Simulation Methods and Algorithms*. Boca Raton, Florida: CRC Press, 1994.
- [31] J. P. Kutter, "Current developments in electrophoretic and chromatographic separation methods on microfabricated devices," *Trends Anal. Chem.*, vol. 19, pp. 352–363, 2000.
- [32] P. D. Fletcher, S. J. Haswell, and V. N. Paunov, "Theoretical considerations of chemical reactions in micro-reactors under electroosmotic and electrophoretic control," *The Analyst*, vol. 124, pp. 1273–1282, 1999.
- [33] S. C. Jacobson, T. E. McKnight, and J. M. Ramsey, "Microfluidic devices for electrokinetically driven parallel and serial mixing," *Anal. Chem.*, vol. 71, pp. 4445–4459, 1999.
- [34] M. H. Oddy, J. G. Santiago, and J. C. Mikkelsen, "Electrokinetic instability micromixing," *Anal. Chem.*, vol. 73, pp. 5822–5832, 2001.
- [35] A. Adjari, "Transverse electrokinetic and microfluidic effect in micro-patterned channels: lubrication analysis for slab geometries," *Phys. Rev. E*, vol. 65, pp. 016301-1–016301-9, 2001.
- [36] T. Thorsen, S. J. Maerkl, and S. R. Quake, "Microfluidic large-scale integration," *Science*, vol. 298, pp. 580–584, 2002.
- [37] M. A. Unger, H.-P. Chou, T. Thorsen, A. Scherer, and S. R. Quake, "Monolithic microfabricated valves and pumps by multilayer soft lithography," *Science*, vol. 288, pp. 113–116, 2000.
- [38] S. Timoshenko and S. Woinowsky-Krieger, *Theory of Plates and Shells*. London, U.K.: McGraw-Hill Book, 1959.
- [39] H. Becker and L. E. Locascio, "Polymer microfluidic devices," *Talanta*, vol. 56, pp. 267–287, 2002.
- [40] J. M. MacInnes, "Current developments in electrophoretic and chromatographic separation methods on microfabricated devices," *Chem. Eng. Sci.*, vol. 57, pp. 4539–4558, 2002.



**Aveek N. Chatterjee** received the B.Tech. degree in mechanical engineering from the Indian Institute of Technology (Kharagpur), India, in 2001 and the M.S. degree in mechanical engineering from the University of Illinois at Urbana-Champaign (UIUC) in 2003, with a minor in computational science and engineering. He is currently working toward the Ph.D. degree at UIUC.

His research interests include computational analysis and design of MEMS, Bio-MEMS and  $\mu$ -TAS, numerical methods in engineering, computational micro/nanofluidics, and bionanotechnological systems.



**N. R. Aluru** (M'00) received the B.E. degree with honors and distinction from the Birla Institute of Technology and Science (BITS), Pilani, India, in 1989, the M.S. degree from Rensselaer Polytechnic Institute, Troy, NY, in 1991, and the Ph.D. degree from Stanford University, Stanford, CA, in 1995.

He is currently an Associate Professor in the Department of Mechanical & Industrial Engineering at UIUC. He is also affiliated with the Beckman Institute for Advanced Science and Technology, the Department of Electrical and Computer Engineering and the Bioengineering Department at UIUC. He was a Postdoctoral Associate at the Massachusetts Institute of Technology (MIT), Cambridge, from 1995 to 1997. In 1998, he joined the University of Illinois at Urbana-Champaign (UIUC) as an Assistant Professor.

Dr. Aluru received the NSF CAREER award and the NCSA faculty fellowship in 1999, the 2001 CMES Distinguished Young Author Award, the 2001 Xerox Award for Faculty Research, and the Willett Faculty Scholar Award in 2002. He is a Subject Editor for the IEEE/ASME JOURNAL OF MICROELECTROMECHANICAL SYSTEMS, Associate Editor for the IEEE TRANSACTIONS ON CIRCUITS AND SYSTEMS II and serves on the Editorial Board of a number of other journals.